

**Project:** 20IND03 FutureCom

**Deliverable:** D1

**Deliverable title:** Good Practice Guide (GPG), summarising the characterisation of active devices and circuits operating under non-50  $\Omega$  loading conditions and for large-signal measurement systems up to 220 GHz.

**Lead Partner:** TU Delft

**Involved Partners:** VSL, TUBITAK, Keysight BE, PTB, NPL, NIBNV

**Due date:** 2024-05-01

**Submission date:** 2024-05-22

# Final Version



## TABLE OF CONTENTS

### Contents

1. Introduction.....	3
2. Active load concept and control.....	4
2.1 $\Gamma$ control resolution identification.....	4
2.2 Active impedance converge in mm-wave test-benches .....	8
3. Calibration procedures and verification.....	10
3.1 Evaluation of power transfer accuracy .....	10
3.2 Waveguide based test benches .....	13
3.3 Power requirements and limitations .....	15
3.4 Non-50 Ohm calibration validation.....	15
4. Good Practice examples .....	16
4.1 Waveguide based test benches Small-Signal .....	16
4.2 Waveguide based test benches Large-Signal.....	17
5. Conclusions.....	19
6. Acknowledgement.....	19

## 1. Introduction

The scope of this guide is to present a set of good measurement practices to be used in non-50 ohm environments, both in coaxial (i.e., up to 65GHz) and in waveguide environments (i.e., WR10, WR6.5 and WR5). Moreover, the guide aims to quantify the measurement advantages (i.e., accuracy and/or uncertainty) that can be achieved by following the proposed approaches.

Among the many possible configurations that have been reported in literature for non-50 ohm large-signal test benches, this guide, will focus only on two implementations of active open-loop load-pull setups, that were studied during the FutureCom project and are shown in Fig. 1a and Fig. 1b, respectively in a coaxial and in a waveguide environment, both configured for CW excitation.

The interested reader that would like a more comprehensive overview of the various load-pull test bench implementations is advised to start with Chapter 13 of [1].

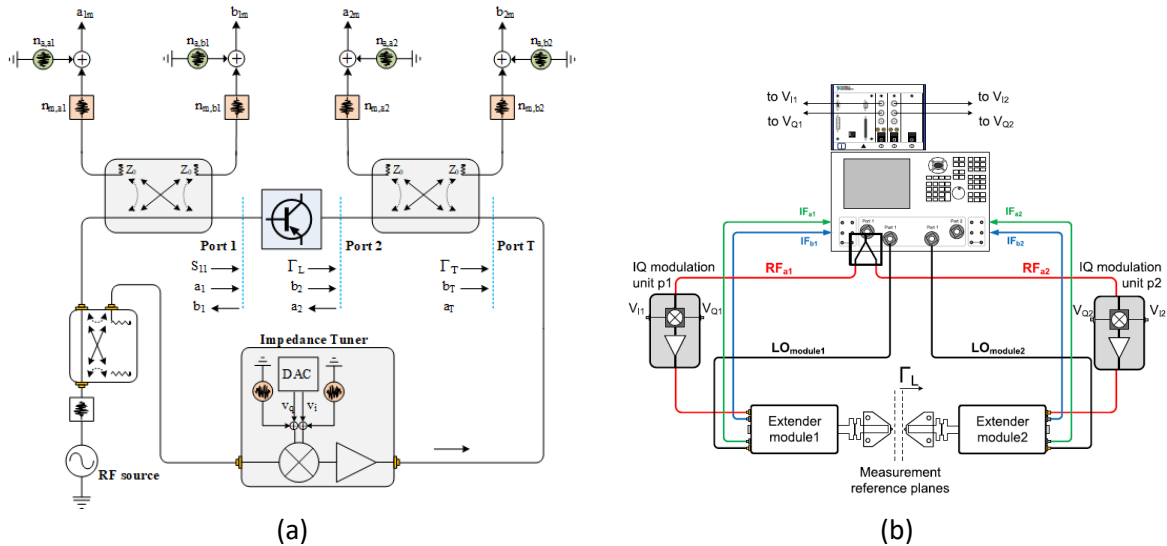


*Fig. 1 Open-loop mixed signal load-pull test benches discussed in the GPG, (a) coaxial implementation supporting only CW measurements [2] up to 20GHz and (b) waveguide on-wafer setup [3] supporting CW and modulated load-pull in waveguide bands from 75GHz up to 500GHz.*

The coaxial measurement system shown in Fig. 1a uses a Copper Mountain VNA (C2420) for large-signal measurement of active devices up to 20 GHz. The coaxial system integrates an in-house designed active (open-loop) impedance tuner based on the vector modulator concept [6]. The impedance tuner sets the load impedance by vector-steering the RF signal using two precision 24-bit digital-to-analog converters (DAC) by the National Instruments Compact Rio platform for sourcing the DC voltages  $v_i$  and  $v_q$ . In addition, precision phase-stable coaxial cables are used to interface with the DUT with minimum measurement errors due to the cable movement. The control and data acquisition of the coaxial measurement system are realized by VSL FAME software designed for large-signal measurements in a Mathworks Matlab environment.

The non-50 Ohm waveguide system shown in Fig. 1b is based on a high performance VNA (i.e., Keysight N5227A) and commercial mm-wave extender modules to provide large dynamic range acquisition of the input and output waves (incident and scattered). A high-precision (i.e. resolution of 83 nV) and low noise (i.e. voltage noise of 6.3  $\mu$ V) digital to analog converter provides the DC signals to a broadband RF IQ modulation unit driven by a single synthesizer source. The increasing multiplication order of

commercially available mm-wave extender modules for the higher waveguide bands allows the use of a unique broadband (passive, diode-based) IQ modulation unit (operating in the 10-20 GHz frequency range), providing system scalability.

## 2. Active load concept and control

Open-loop active loads, based on the mixed-signal concept introduced in [4], are based on signals generated by baseband AWGs (digital-in/analog-out, thus the mixed signal name) and up-converted, to the desired RF frequency, using IQ mixers. As in the classical open-loop approach, also in the mixed signal open-loop case, the final result (user-defined reflection coefficient) is obtained by iteratively adjusting the amplitude and phase of the injected waveforms independently at each frequency and power level of interest. Within the scope of this GPG, only single tone (CW) excitation will be considered.

The interested reader who would like to learn more about broadband load-pull realization in coaxial environments is suggested to start from Chapter 14 of [1].

Given the non-linear nature of the DUT (i.e., transistor or circuit operating in the moderate to strong non-linear regime) the iteration procedure i.e., the number of iteration steps, is defined by the predictive behavior of the convergence algorithm and the convergence criteria (i.e., acceptable vector distance to the user-defined value). The following sections describe good practice approaches for determining the gamma control resolution (which provides indication on how to select the convergence criteria) and required constraints to be used in RF and mm-wave load-pull benches.

### 2.1 $\Gamma$ control resolution identification

In this section, we describe a procedure to quantify the measurement noise in the reflection coefficients synthesized via mixed-signal active tuners. The setup of Fig. 1a will be used to describe this procedure, which can also be applied to a waveguide setup as the one shown in Fig. 1b.

This noise contribution is an important parameter for the determination of the convergence algorithm resolution capability and when attempting to implement a complete uncertainty propagation in active load-pull test benches.

The noise sources involved in vector network analyzer (VNA) measurements can be grouped into two main categories, i.e., additive noise  $\sigma_a^{\square}$  and multiplicative noise  $\sigma_m^{\square}$  sources. While [5] identifies VNA measurement noise contribution as marginal, it is a critical factor in measurements demanding high-resolution performance [6]. A measurement noise model identifying  $\sigma_a^{\square}$  and  $\sigma_m^{\square}$  noise sources in a VNA by [6] is shown in eq. 1 and eq 2.

$$\sigma|\Gamma_T| = \sigma_a + \sigma_m|\Gamma_T| \quad (1)$$

$$\sigma\angle\Gamma_T = \tan^{-1}\left(\frac{\sigma_a}{|\Gamma_T|}\right) \quad (2)$$

These noise sources have an inevitable interdependence (correlation) due to, for example, the shared source signal and the local oscillator (LO) of both down-conversion chains. However, here, both noise sources are assumed uncorrelated, as the detailed noise comparison, presented in [6], between the noise values acquired with the proposed noise model and the measured values showed differences of less than 10 % throughout the entire  $\Gamma$ -measurement range and were deemed adequate.

The procedure for characterizing active impedance tuner noise involves the following steps:

1. Characterizing the transfer function of the mixed-signal tuner.
2. Digital to analog converter (DAC) noise evaluation.
3. Mixed-signal tuner noise evaluation.

#### Step 1: Characterizing mixed-signal tuner transfer function

The reflection coefficient synthesized by the active tuner is a function of the  $V_I$  and  $V_Q$  DC voltage values and is referred to as the active tuner's transfer function. First, the transfer function of the active tuner is determined by mapping the provided reflection coefficient as a function of the  $V_I$  and  $V_Q$  DC voltage values.

To obtain the above-mentioned transfer function, the VNA is calibrated using a short-open-load (SOL) calibration method using traceable 3.5 mm coaxial standards. The measurement system is calibrated at several frequencies ranging from 2 GHz up to 18 GHz with 4 GHz steps, as this is also the operational frequency range of the active tuner. Subsequently, the calibrated tuner reflection coefficient  $\Gamma_T$  is measured for a range of  $V_I$  and  $V_Q$  DC voltage values. These voltages represent the baseband signals (in the case of a CW tuner these are DC voltages) applied to the upconverter. The magnitude of the chosen IQ vector for the characterization ranges from 0.1 mV up to 0.08 V, with a logarithmic distribution. We sweep the equivalent phase of the upconverted vector ( $\angle IQ$ ) from 0 to 360 degrees at each IQ-magnitude value with a 45-degree step size. The results are shown with red markers in Fig.2.

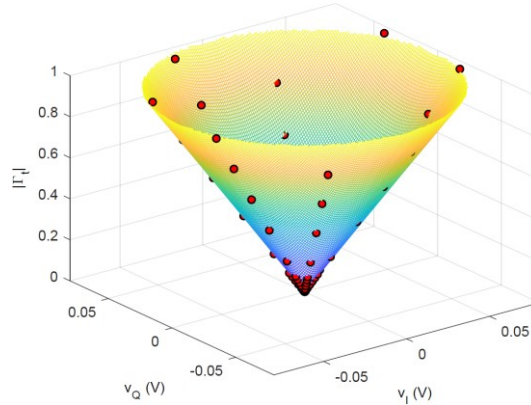


Fig. 2: The IQ-mixer transfer function results for the magnitude component at 4 GHz. The markers in red are the measurement values, and the colored area is the results acquired with the model based on the polynomial fit of the measurement values.

Subsequently, polynomial fits of the measurement results, shown in Fig. 2 with colored area, are determined to model the corresponding behavior with closed-form equations. These closed-form equations allow calculating the sensitivity coefficients between the IQ-baseband voltages and the tuners  $\Gamma_T$  needed for uncertainty propagation. The polynomial expressions used to fit the data are described in eq. 3 and eq. 4.

$$|\Gamma_T|(|IQ|, \angle IQ) = a_0 + \sum_{n=1}^5 \left( |IQ|^n \sum_{m=1}^2 \angle IQ^m b_m \right) \quad (3)$$

$$\angle \Gamma_T(|IQ|, \angle IQ) = c_0 + \sum_{n=1}^5 \left( |IQ|^n \sum_{m=1}^2 \angle IQ^m d_m \right) \quad (4)$$

Here, we chose to use the magnitude ( $|IQ|$ ) and phase ( $\angle \Gamma_T$ ) of  $V_I$  and  $V_Q$  DC voltage values, as this allows the direct interpretation of the magnitude and phase variations, introduced by the  $V_I$  and  $V_Q$  driving voltages and then subsequently measured for tuner's  $\Gamma_T$ . The modulus and phase of the reflection coefficient dependency on the baseband IQ vector are then incorporated in the Jacobian matrix shown in eq. 5.

$$J_T = \begin{bmatrix} \frac{\partial |\Gamma_T|}{\partial |IQ|} & \frac{\partial |\Gamma_T|}{\partial \angle IQ} \\ \frac{\angle \Gamma_T}{\partial |IQ|} & \frac{\angle \Gamma_T}{\partial \angle IQ} \end{bmatrix} \quad (5)$$

Finally, using the covariance matrix containing the IQ-baseband noise values shown in eq. 6 and the Jacobian matrix, determined in eq. 5, we can calculate tuner reflection coefficient noise using eq. 7.

$$\Sigma_{IQ} = \begin{bmatrix} \sigma_{|IQ|}^2 & c_{IQ} \\ c_{IQ} & \sigma_{\angle IQ}^2 \end{bmatrix} \quad (6)$$

$$\Sigma_T = \begin{bmatrix} \sigma_{a,m}^2 & c_{IQ} \\ c_{IQ} & \sigma_{a,p}^2 \end{bmatrix} = J_T \cdot \Sigma_{IQ} \cdot J_T^T \quad (7)$$

Here,  $\sigma_{a,m}^2$  and  $\sigma_{a,p}^2$  are the additive noise in the magnitude and phase components, and  $c_{IQ}$  is the correlation coefficient between magnitude and phase component. The impact of ignoring the correlation is marginal, as evident from Fig. 4, when using the magnitude and phase components instead of propagating noise on the  $V_I$  and  $V_Q$  DC voltage values. As it concerns an additive noise source, the phase of the noise vector is considered to be within 0 and 360 degrees with an equal probability. Hence, the effect of  $\sigma_{a,p}^2$  is negligible as  $\sigma_{a,m}^2$  will set the noise-floor.

#### Step 2: DAC noise evaluation

Once the transfer function of the impedance tuner is determined, then the noise corresponding to the of  $V_I$  and  $V_Q$  DC voltages generated by the DAC is to be measured. Subsequently, the DC noise values  $\sigma_{|IQ|}^2$  and  $\sigma_{\angle IQ}^2$  corresponding to  $V_I$  and  $V_Q$  are propagated using the proposed method for calculating the corresponding  $\Gamma_T$  reflection coefficient noise.

#### **DC noise measurements**

In this example, we use a multi-channel NI-9260 DAC that provides the DC voltages  $V_I$  and  $V_Q$  needed to control the tuner  $\Gamma_T$ . The DAC has two voltage output channels with a 24-bit analogue output resolution and a sampling rate of 51.2 kS/s. The DC noise levels of the I-channel ( $\sigma_I^2$ ) and Q-channel ( $\sigma_Q^2$ ) are measured to determine the noise contribution of the DAC. For that, DC voltages  $V_I$  and  $V_Q$  were generated and measured using an HP-3458A multimeter. Different integration times were set in the multimeter, and 1000 samples were collected for each voltage and integration time. Because the integration time acts as a low-pass filter for the noise, the equivalent cutoff frequency is calculated by taking the inverse of the integration time. The noise is calculated by taking the standard deviation of the samples recorded. Fig. 3 depicts the noise results for ( $\sigma_I^2$ ) and ( $\sigma_Q^2$ ) as the standard deviation versus the equivalent integration frequency. The noise is measured for three different  $V_I$  and  $V_Q$  values covering the range of  $\Gamma_T$  values that the active tuner will generate. The noise remains similar for the three voltage levels tested; above the 10 kHz, it shows a dependency on the voltage level set at the DC source. The level below 1KHz shows a flat response and is the value considered for the following steps.

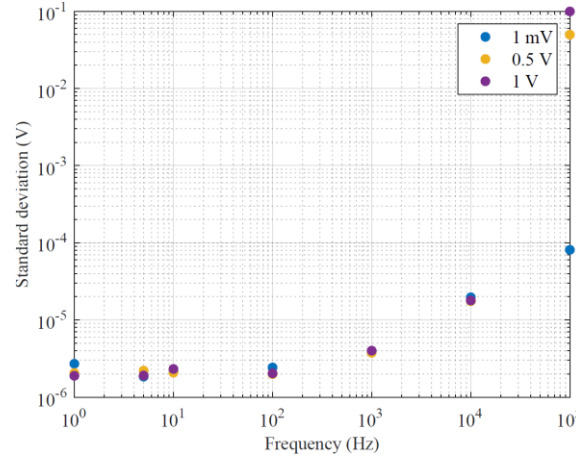


Fig. 3 DC source noise measurement results for I and Q channel DC voltages as function of equivalent integration frequency.

### Step 3: Mixed-signal tuner noise evaluation

This section provides the validation of the proposed method. The final step involves characterizing the reflection coefficient measurement noise when the mixed-signal tuner is employed. The VNA test-port power level is set at -10 dBm, an intermediate frequency bandwidth (IFBW) is set at 7 Hz. Subsequently, the tuner is connected to the VNA and set to generate reflection coefficients ranging from 0 to 1 using  $V_I$  and  $V_Q$  signals provided by the NI DAC. At each tuner  $\Gamma_T$  value, 1000 samples are acquired from the VNA. The calibrated data is then used to calculate the standard deviation and shown with red markers in Fig. 4b and Fig. 4c.

After, the characterized noise  $\sigma_{|IQ|}^2$  is propagated onto the generated reflection coefficient  $\Gamma_T$  using eq.7. For this, the input covariance of eq. 6 is determined by assuming  $\sigma_I^2$  and  $\sigma_Q^2$  noise of 2.1  $\mu$ V for  $V_I$  and  $V_Q$  baseband signals. The calculated additive noise  $\sigma_{a,m}^2$  is then used in eq. 1 and eq. 2 to predict the  $\Gamma_T$  noise, shown in Fig. 4 with dotted lines. Furthermore, the multiplicative noise is estimated using highly mismatched reflection coefficient measurements. Fig. 4 shows the comparison results between the measurement and calculated noise values, demonstrating the predicting behavior of the noise model, which can be employed to identify the noise of the active load at different impedance levels.

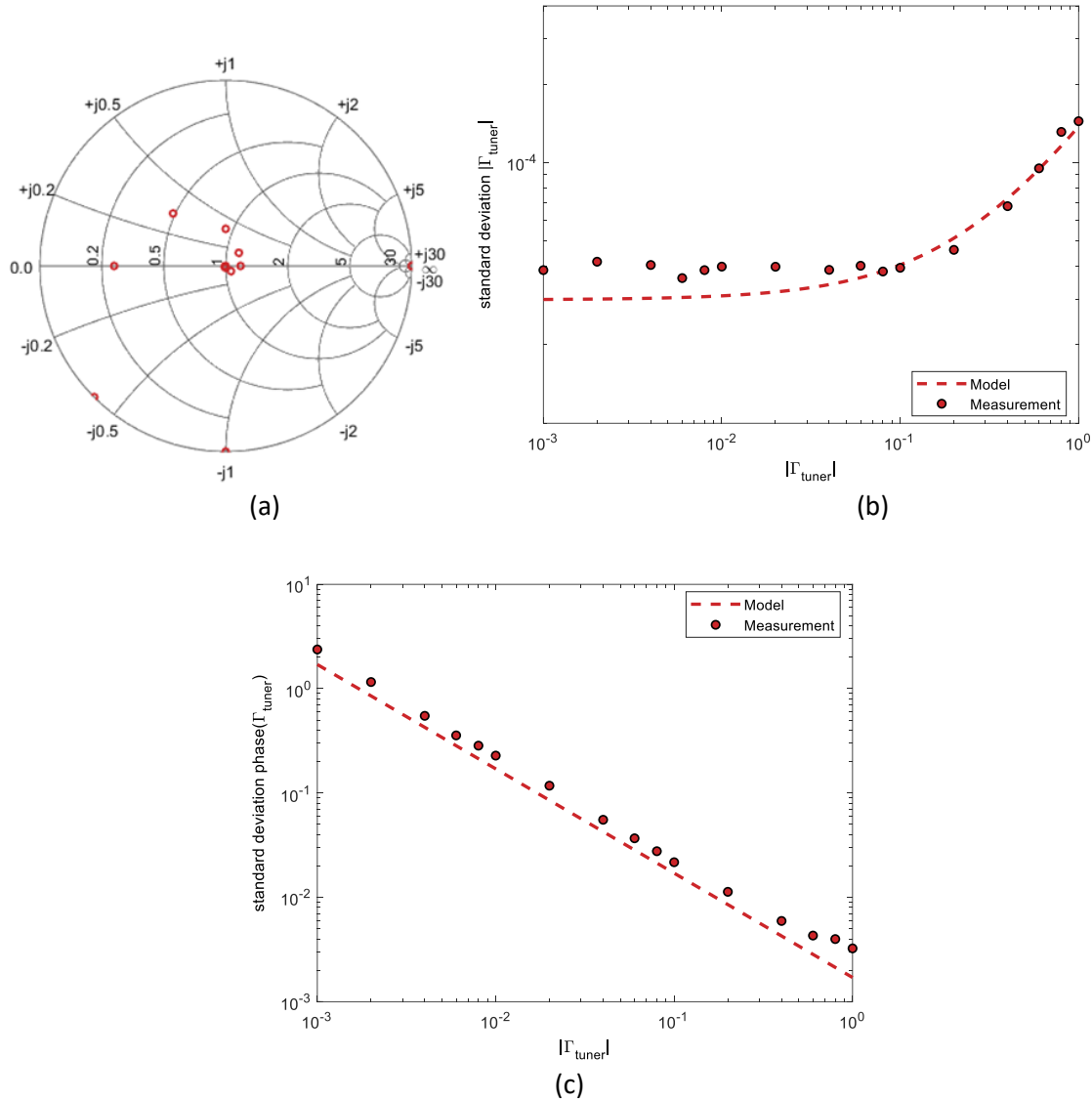


Fig. 4: Noise measurement results for active impedance tuner. (a) Shows the measured impedance values in a 50 Ω normalized Smith chart. (b) Shows noise results for reflection coefficient magnitude. (c) Shows noise behavior for the reflection coefficient phase.

## 2.2 Active impedance converge in mm-wave test-benches

When considering mm-wave test benches it is important to mention that the control of the injected wave to synthesize the user defined reflection coefficient is realized at a frequency (N times) lower than that of the DUT, with N being the VNA extender multiplication order which is vendor and waveguide band specific.

### Convergence problems

Since the frequency (up)scaling of the wave to the DUT frequency range is achieved via the non-linear (harmonic) process realized by the mm-wave extenders a non-linear behavior in the transfer function between RF to mm-wave is realized, which adds a complexity layer to the convergence algorithm. This can be shown by 3D plotting the reflection coefficient behavior versus the control (mixed-signal voltages), for the fundamental case (N=1) and a higher multiplication order case (N=12), see Fig. 5.



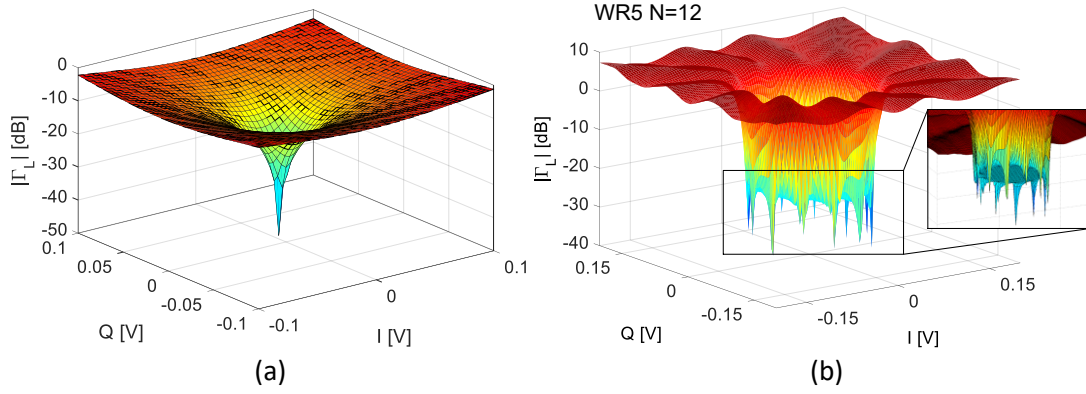


Fig. 5: . Magnitude of  $\Gamma_L$  versus IQ bias settings for: a) injected wave control at the fundamental (DUT), b) injected wave control at the sub-harmonic frequency ( $N$  times smaller than DUT frequency). The plot is obtained for a single  $\Gamma_L$  target, but can be replicated for any wanted reflection coefficient and does provide a similar surface shape characteristic.

Given that most convergence algorithms employed in open-loop load-pull test-benches make use of derivate-based iterations to reach convergence, it is important to note that when large, flat regions are present, as is the case of Fig. 5b, can lead to convergence problems since in those areas the solution would be undefined. To overcome this limitation, when aiming at implementing iterative (i.e., open-loop) load-pull test benches operating at a multiplied frequency, constraints to the possible variation of the input variables (i.e., in this case  $I$  and  $Q$  DC signals) need to be implemented.

As an example in Fig. 6, the constraints to two sub regions on the variability of the  $I$  value is shown.

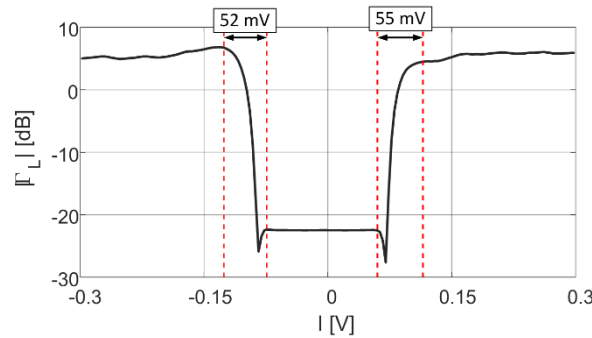


Fig. 6: Cross section of Fig. 5b, where  $Q$  is kept constant and the constrained regions to avoid the zero derivate conditions are shown.

### Device failure conditions

When considering open-loop approaches it is important to understand that the initial injected wave is completely set by the user, and thus not related at the hardware level to the wave emitted, at its output, by the DUT.

For this reason, when no prediction/scaling is implemented to the injected wave to an (indicative) appropriate value required to synthesize the chose reflection coefficient there is an effective risk to synthesize loading conditions that might damage the device.

To identify the level of the wave emitted from the DUT, as a first order approximation, the small signal  $S_{21}$  of the device can be used in conjunction with the drive level applied at the input. This step allows to identify the magnitude level of the wave emitted by the DUT at the calibration reference plane. To predict the amplitude and phase level of the injected wave a model of the active tuner as described in section 2.1 can be used. This approach allows to constrain the load impedance to a small set of value

closed to desired value, see Fig. 7a and avoids that the convergence algorithm uses load conditions, during the search, which can lead to instabilities or damage of the DUT, see Fig. 7b.

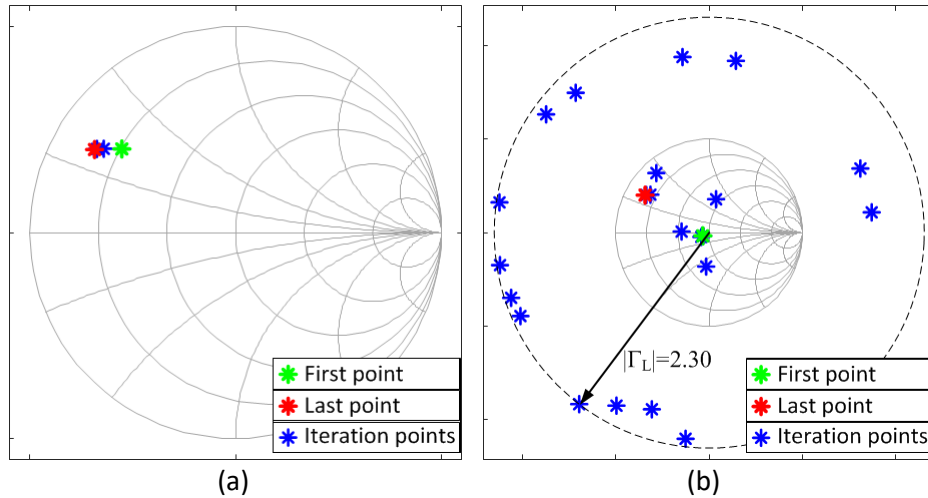


Fig. 7: Convergence path of  $\Gamma_L$  during the convergence using: the algorithm with prediction a) and without the prediction b).

### 3. Calibration procedures and verification

The large signal non-50 Ohm test bench calibration is performed in two steps.

First, a reflection coefficient (one or two port) calibration is performed following the same requirements and achievable performance of classical small-signal VNA test benches. After, an absolute power calibration is performed to map the power level from a power detector to the receiver of the unit being used (i.e., VNA), following the approach presented in [8] and [10]. Depending on the frequency of the test bench, this second calibration can be performed also in on-wafer environments without breaking the calibration path (i.e., coaxial fundamental test-benches), or it is carried out at a connectorized interface (i.e., waveguide flange) and after the probing interface is added, needs to account for this extra network that is to be removed to bring the power level reference plane at the probe tip (i.e., waveguide based test-benches).

The reader is referred to the following papers to identify the procedure required for the calibration steps:

- 1) Coaxial fundamental test-benches: REF [A. Ferrero and U. Pisani, "An Improved Calibration Technique for On-Wafer Large Signal Transistor Characterization", IEEE Trans. Instrum. Meas., vol. IM-47, pp. 260-364, Apr. 1993.]
- 2) Waveguide multiplied test-benches: REF [L. Galatro, S. Galbano, A. Santaniello and M. Spirito, "Power control for S-parameters and large signal characterization at (sub)-mmWave frequencies," 2015 85th Microwave Measurement Conference (ARFTG), Phoenix, AZ, USA, 2015, pp. 1-4].

#### 3.1 Evaluation of power transfer accuracy

This section presents guidelines on the power calibration and linearity evaluation of VNA measurement receivers. Two power calibration methods are explained and compared, providing an overview of the advantages and drawbacks associated with both methods. The measurement receiver power calibration allows to measure and control input power offered to the device under test (DUT). An important consideration in power sensor calibration with a VNA is susceptible to measurement errors due to the presence of harmonics. Dedicated filter banks are employed in power sensor calibration

setups at NMIs to reduce the impact of signal harmonics on the measurement results. However, this is not possible in VNA-based power calibration of broadband power sensors and requires detailed uncertainty evaluation.

The first power calibration method, known as the direct-comparison transfer (DCT) technique shown in Fig. 8a [7], performs power calibration with measurements performed in pairs, i.e., a traceable power sensor or DUT is measured simultaneously with a VNA a-receiver. Here, the DUT measures ( $P_{DUT}$ ) simultaneous with a monitor power sensor ( $P_{M,DUT} = |a_m|^2$ ), which is the VNA a-receiver measurement. Subsequently, the DUT is replaced with a traceable power sensor ( $P_{REF}$ ) and completed identical measurement with the monitor ( $P_{M,REF}$ ). These measurements are combined in the following (1) to determine the DUT calibration factor:

$$K_{DUT} = K_R \frac{P_{DUT}}{P_{M,REF}} \frac{P_{M,DUT}}{P_{REF}} \frac{|1 - \Gamma_{DUT} e_{11}|}{|1 - \Gamma_{REF} e_{11}|} \quad (1)$$

Here,  $K_R$  is the calibration factor of the reference power sensor and  $e_{11}$  the VNA source match term. The advantage of the direct comparison method is the insensitivity towards signal source variations, as these are cancelled out with the VNA a-receiver employed as a monitor power sensor. However, the technique does require two sequential measurement rounds to transfer the power calibration onto the DUT.

The second method is the feed-through (FT) technique based on [8] and also described in [9]. Here, the VNA a-receiver is measured simultaneous with the DUT. Using the VNA for FT-based calibration requires (first) calibrating the incident-wave ( $a_m$ ) measurement receiver, see Fig. 8 for a flow graph of the VNA-based power transfer standard. The following eq. 9 is used to determine DUT calibration factor using a VNA.

$$K_{DUT} = K_{am} \frac{P_{DUT}}{P_{am}} |1 - \Gamma_{DUT} e_{11}| \quad (9)$$

where  $P_{DUT}$  is the power measured by the DUT sensor,  $P_{am}$  (monitor) is the power measured at the receiver 'a<sub>m</sub>',  $K_{am}$  is the calibration factor of the VNA 'a<sub>m</sub>' receiver and  $\Gamma_{DUT}$  is the DUT input reflection coefficient.

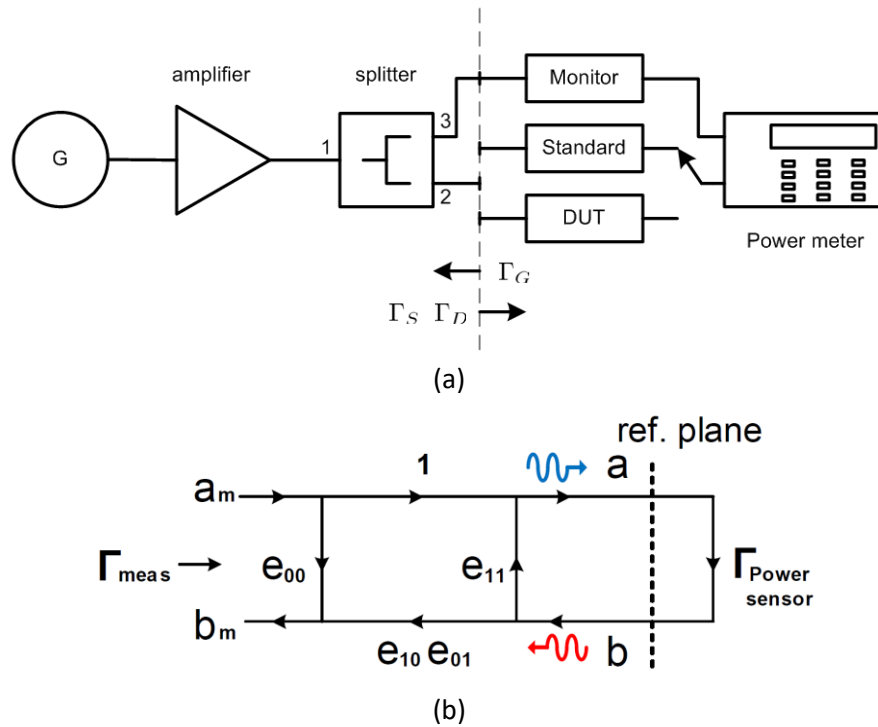
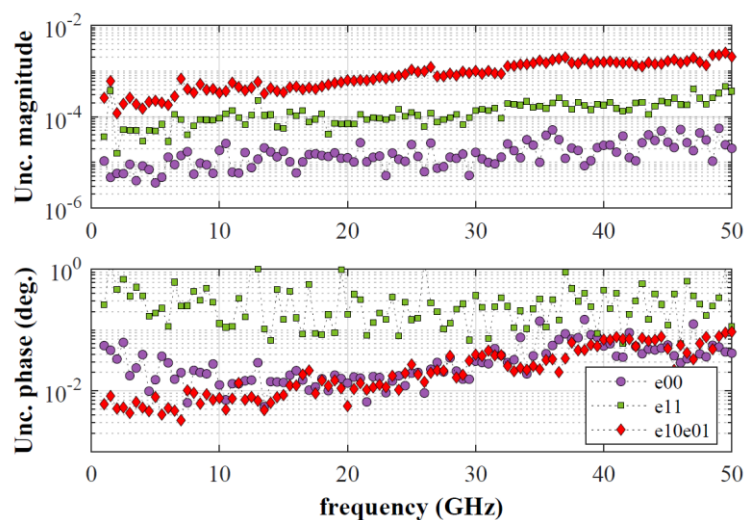


Fig. 8 (a) Overview of the direct-comparison power calibration setup. (b) Flow-graph of the VNA-based power sensor calibration setup.

### Practical use-case

The following experiment is designed to estimate the deviation of all three error terms (see Fig. 8b) while sweeping the signal power level from +10 dBm to -30 dBm with 10 dB steps. First, 2.4-mm mechanical short-open-load (SOL) calibration standards are successively measured with a VNA from 10 MHz to 50 GHz for the selected signal power levels. This reduces the number of connections for each device to a single connection, excluding connector repeatability effects. Once all three devices are measured, the VNA error terms are calculated for every power level. Finally, the uncertainty of every error term due to varying the incident signal power level from +10 dBm to -30 dBm is calculated with the standard deviation of all power level data. The error term uncertainty values related to the test port power level are shown in Fig. 9.



*Fig. 9 VNA error-term uncertainties due to incident signal power level ranging between -30 dBm to +10 dBm.*

Subsequently, VNA's ability to serve as a high dynamic range monitor sensor is investigated for calibration factor (CF) measurements using the direct-comparison transfer method. A 2.4-mm power sensor (DUT) is calibrated using two reference power sensors, identified as reference A and reference B. Here, reference A sensor provides a traceable calibration factor for 0 dBm power level, while reference B sensor provides a traceable calibration factor for -30 dBm power level. Fig. 10a depicts the DUT calibration factor results determined at +10 dBm to -20 dBm using reference A, and at -20 dBm when using reference B. The DUT shows excellent agreement between these two approaches, with calibration factor errors substantially smaller than the corresponding reference value uncertainties. Finally, the VNA capability to act as a high dynamic range power transfer standard is evaluated by calibrating a DUT sensor using the a-wave measurement receiver of the VNA. The VNA measurement receiver is first calibrated at 0 dBm power level using reference A. Subsequently, the DUT sensor is calibrated at power levels +10 dBm to -20 dBm using the VNA a-wave receiver calibration factor with the feedthrough method, with the results as shown in Fig. 10b. The VNA results are comparable to the direct comparison method up to -10 dBm, while showing marginally larger errors for -20 dBm power level.

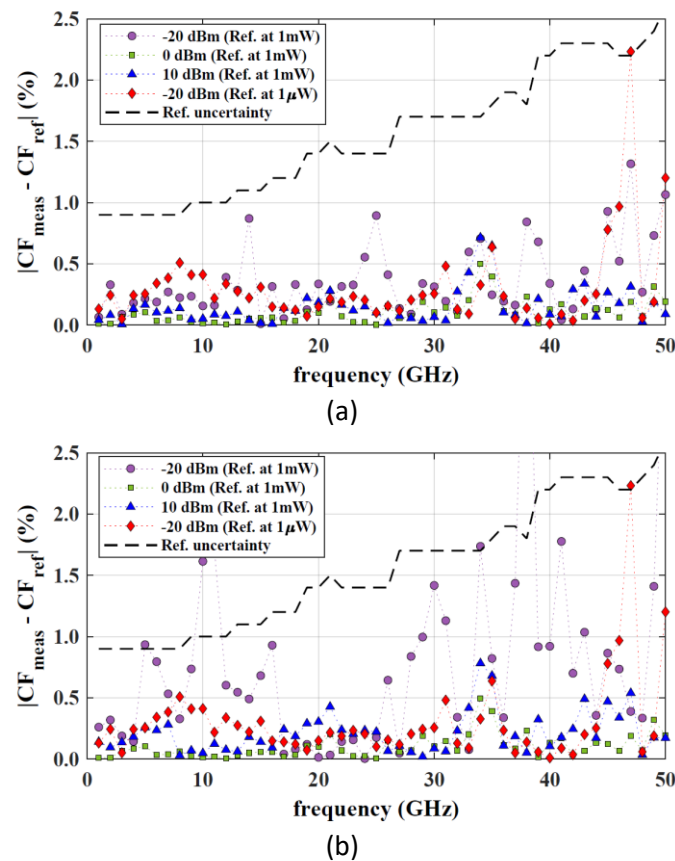
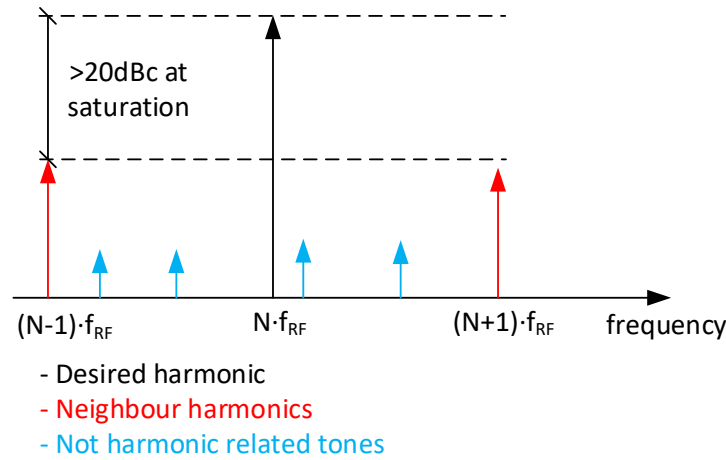


Fig. 10 (a) DUT calibration factor comparison between the measurement results and reference values. The calibration measurements are performed using the direct-comparison transfer method with a VNA. (b) DUT calibration factor comparison between the measurement results and reference values. The calibration measurements are performed using the feed-through method with a VNA.

### 3.2 Waveguide based test benches

Waveguide large signal test benches as the one presented in Fig. 1b employ pre-multiplier modulation to realize the synthesized reflection coefficient at the output port and the user defined power sweep at the device input.

It is important for the operator to realize that given the non-linear nature of the multiplication process, a number of harmonically-related and other spurious signals will be present in the frequency band covered by the extender module, as is schematically depicted in Fig. 11.



*Fig. 11: Typical output spectral content of a frequency extender.*

When varying the input power to the multiplier (i.e., backing off from saturation) can (possibly) degrade its nominal response in terms of spectral harmonic rejection. For this reason, it is a good practice to identify the “quasi-CW” range in which a given frequency extender module can be used. The term “quasi-CW” refers to the case when the total amount of power present in the unwanted harmonics is below a selected (user-defined) level.

To identify this range after the power calibration of the test-bench has been performed, the spectral power at each (cal) frequency point (i.e., acquired with the VNA) is compared with the average power acquired with a broadband power detector (i.e., RMS power meter) following the approach described in [10].

The examples presented in this guide for the “quasi-CW” range evaluation have been performed using a Keysight PNA N5224B, WR10 frequency extenders employing WR10 AMC-I and WR6.5 VDI multipliers and operating the entire system via the MMW-STUDIO software provided by Vertigo Technologies. The broadband power detector is a calorimeter-based power meter, i.e., the VDI Erikson PM5.

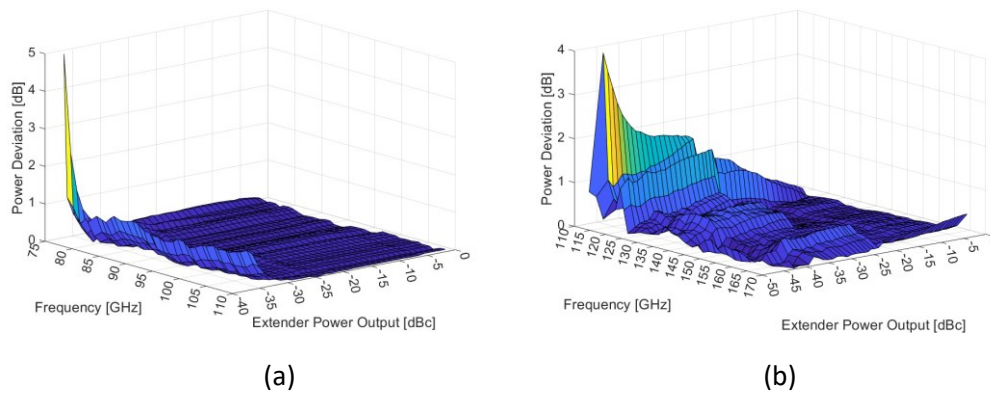


*Fig. 12: Difference between fundamental power and integrated power for WR10 a) and WR6.5 b) mm-wave extenders for various output levels. The “quasi-CW” range should be defined by the user as the maximum acceptable power deviation.*



As can be seen in Fig. 12 at increasing back off level from the multiplier saturated power (i.e., 0 dBc in the axis of the figures) the distance between the spectral power (i.e., measured by the narrowband VNA receiver after calibration) and the total power increased. This increase will be strongly frequency and manufacturer dependent, for this reason the user is advised to run this comparative analysis before performing any measurement that employs wave amplitude control by varying the input power to the multiplier. The specific value of the power deviation can be set by the user, a practical limit value should not be below 1 dB.

### 3.3 Power requirements and limitations

Active load-pull test bench require (large amounts of) power to be injected towards the DUT to realize high  $|\Gamma|$  conditions. When moving to mm-wave (i.e., waveguide based test benches) the scarce availability of commercial medium/high power amplifiers and pre-matching tuners (especially above 110 GHz) implies that extreme  $|\Gamma_L|$  cannot be reached for medium/high power transistor cells.

In order to evaluate the maximum  $|\Gamma_L|$  condition that can be obtained in a given test-bench the operator can use the simple formula presented in [11] and shown in the inset of Fig. 13.

The formula provides a best case scenario as it does not include (eventual) losses between the active tuner element and the DUT plane.

When employing the formula of [11] considering the (Pmax) usually reported values for mm-wave extender modules operating in the WR6.5 bands and above we can see that when the devices is providing more than -10 dBm, conventional frequency extenders are not able to reach  $|\Gamma_L|=1$ .

For this reason, an important good practice approach is to always evaluate the maximum achievable reflection coefficient that can be obtained with a given test bench for the output power expected by the DUT.

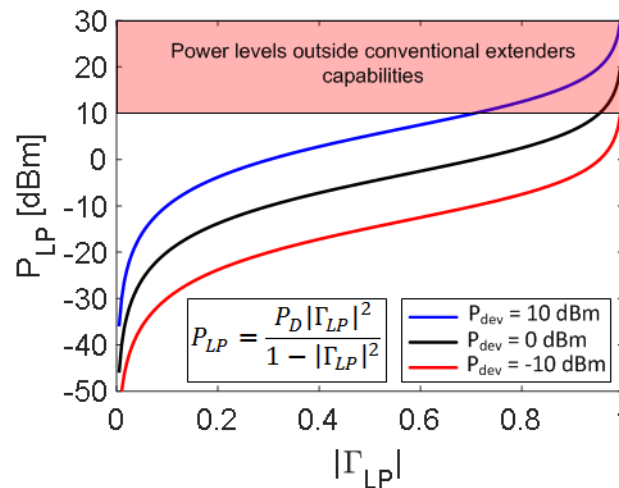


Fig. 12: Power required from the output source to emulate a defined  $|\Gamma_L|$ , for different device output power (i.e., related to the power cell size, and indicating what is a power range achievable by commercial extender modules (i.e., indicative number for WR5/WR10 waveguide bands).

### 3.4 Non-50 Ohm calibration validation

As was discussed in [12] the residual calibration uncertainty on absolute-power-level measurements can impact strongly the accuracy of the classical non-linear metrics used to characterized non-linear devices in non-50 Ohm environments.

A good approach to identify the residual calibration uncertainty in a quantifiable way is to compute a chosen large signal metric, for varying  $\Gamma_L$ , on a passive device. This approach allows to quickly and accurately identify the limit of non-50 Ohm loading conditions to employ, given a user chosen uncertainty level. It is important to mention that this level should be related to the uncertainty level of absolute wave measurements, which is well above the expected uncertainty levels of linear S-parameters. An example of levels of uncertainty under difference  $\Gamma_L$  circles, in WR 5 band (i.e., 180GHz) is shown in Fig. 13.

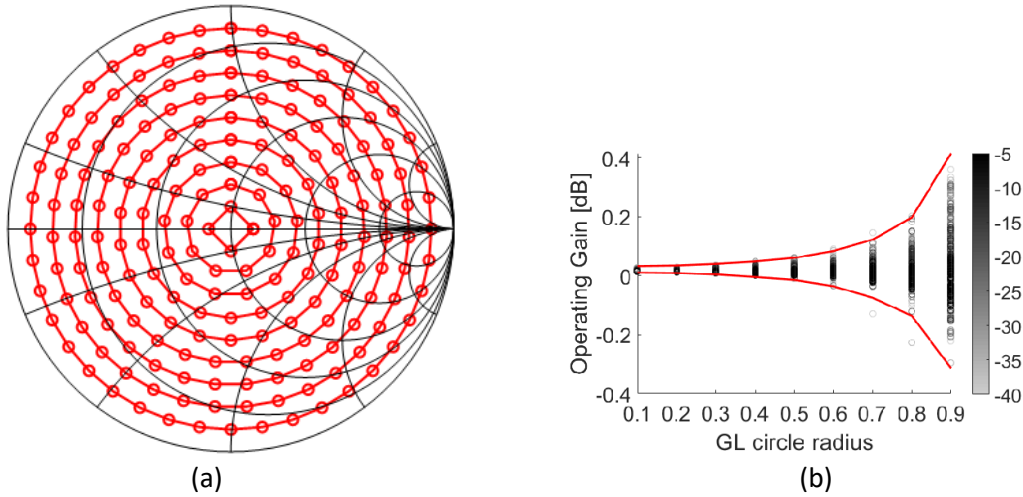


Fig. 13: a)  $\Gamma_L$  points measured on the circles at different modules to get the gain test and generate Fig. 11c. b) Operating gain versus the  $\Gamma_L$  modules for the points shown in Fig. 11b. It is measured on a thru connection at 180 GHz at various power levels (i.e., from -40 dBm to -5 dBm, right intensity scale). The red lines represent the  $3\sigma$  (i.e., 99%) confidence bounds.

It is important to mention that these accuracy levels can be further improved means of error terms optimization, the interested reader is invited to read [13] for further information on this approach.

## 4. Good Practice examples

### 4.1 Waveguide based test benches Small-Signal

In Section 3 the approaches to transfer the power calibration to the VNA receivers and thus to achieve vector corrected absolute levels of the incident and scattered waves at the input and output of the device were introduced. When attempting to measure active devices in the mm-wave ranges, where the test-bench employs WNA extender modules (as the ones shown in Fig. 1b), it is important to understand that the non-linear frequency tracking of the output power of the extenders (see Fig. 14) can introduce AM/AM distortion in the device response (even in small-signal measurements) which are transferred by the characteristics of the test-bench.



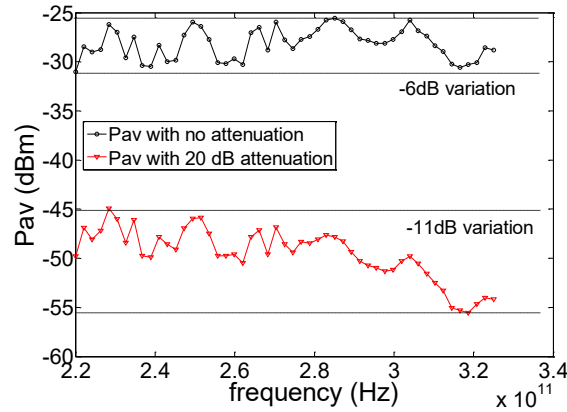


Fig. 14: Output power versus frequency of a mm-wave extender module in the WR-03 range, at different value of external attenuation.

To show this effect an 140 GHz PA is considered as a test vehicle. When no power calibration and SW based power control is applied during the measurement procedure, an unknown power level with a large power fluctuation across the waveguide band can occur, see Fig. 15a) red trace.

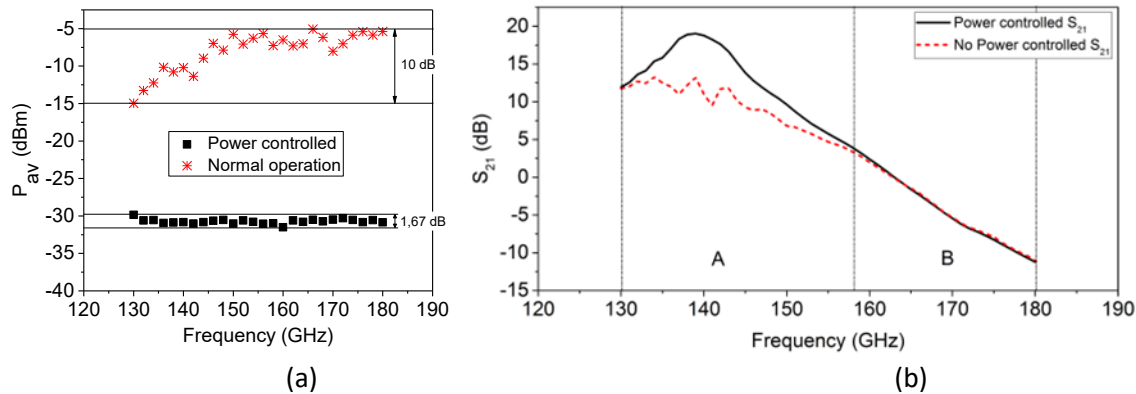


Fig. 15: a) power output from the WR5 module, b)  $S_{21}$  of a D-band PA measured when no-source power control is applied (dashed line) versus the case with -30 dBm controlled  $P_{av}$  (solid line).

This non-linear frequency tracking of the input wave to the DUT can transfer the source non-linearity into an AM/AM distortion in the device metric. This incorrect response is very difficult to occur in coaxial test bench where automatic level control (ALC) of the synthesizer power is available up to the VNA test port, and a very fine power level control is always available to test the device response.

## 4.2 Waveguide based test benches Large-Signal

When aiming to employ load-pull test benches for model validation and or device optimization for a given parameter it is important to tune the higher harmonic terminations when possible (i.e., coaxial load-pull test benches [15]), or to identify the system (passive) termination at those frequency and use them in the simulation environment for improved model to hardware correlation.

At mm-wave frequencies, when employing waveguide probes, the out of band impedance terminations are defined by the combination of the waveguide impedance at those frequencies and the e-probe/radial-probe used within the wafer probe, see Fig. 16, to transform the waveguide mode in the chosen transmission line one.

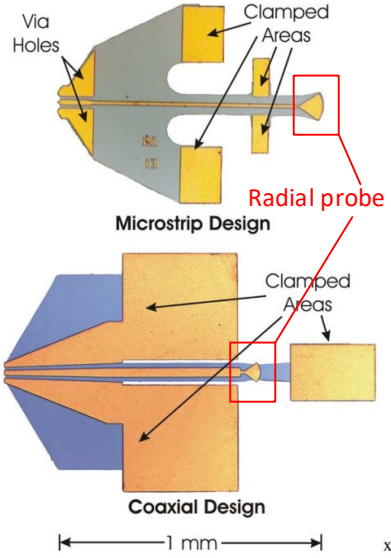


Fig. 16: Photomicrographs of the microstrip and CPW-based probe chips, adapted from [14] to highlight the radial probe section.

The out of band termination of the probe can be acquired in a separate set of one-port measurement where the input used the correct VNA extender module to derive the load reflection value at  $2f_0$  and  $3f_0$ . After this characterization step is performed the non-50Ohm system can be mounted as shown in Fig. 1b, and the load pull measurement carried out. An example of device level load-pull measurements with fundamental drive at 75GHz are shown in Fig. 17.

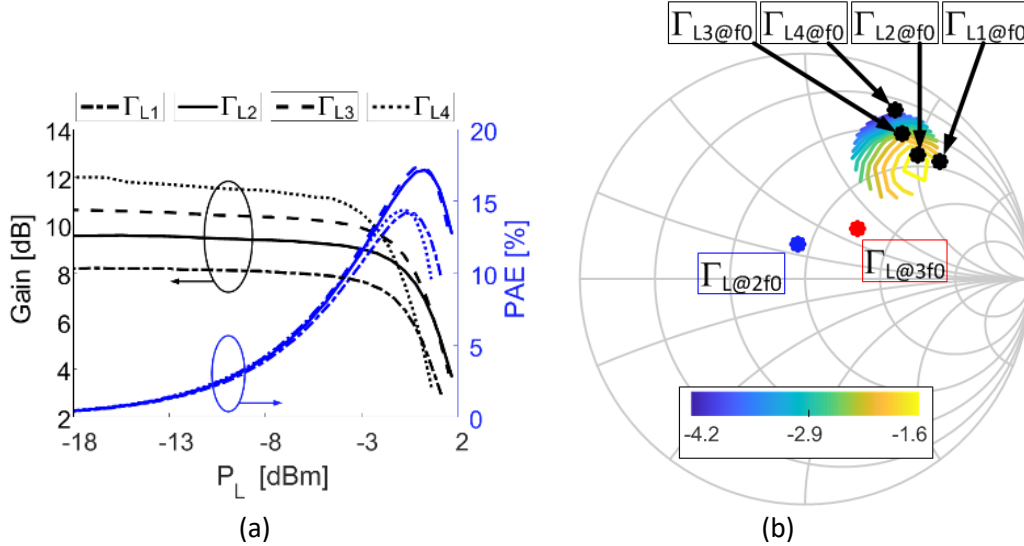


Fig. 17: Load-pull measurement results on IHP microelectronics SG13G2 130 nm HBTs at 75 GHz. a) Gain and Power Added Efficiency (PAE) sampled in 4  $\Gamma_L$  points distributed from the lowest to the highest gain value point. b) Contour plot showing the PL constant circle and the 2 harmonic passive impedances ( $\Gamma_L @ 2f_0 = -0.032+j0.155$ ;  $\Gamma_L @ 3f_0 = 0.233+j0.224$ ). Moreover the 4  $\Gamma_L$  points position are highlighted ( $\Gamma_{L1} @ f_0 = 0.597+j0.512$ ;  $\Gamma_{L2} @ f_0 = 0.495+j0.550$ ;  $\Gamma_{L3} @ f_0 = 0.435+j0.636$ ;  $\Gamma_{L4} @ f_0 = 0.409+j0.744$ ).

Given the complexity of integrated circuit design at frequencies above 100 GHz, arising from the strong impact of the layout associated parasitic, load-pull test benches can also be employed to further tune the load termination of a matched PA. This measurement provides to the designer important feedback on the quality of the EM (back-end-of-line) simulation quality, and highlights if more power can be “pulled out” of the device.

In Fig. 18, the PA of [16] is load-pulled at the fundamental frequency of 135GHz to identify possible gains in  $P_{out}$  compared to the 50 Ohm case. As can be seen by Fig. 18a, the optimal load condition for  $P_{out}$  is located quite distant from the center of the Smith chart, thus highlighting some inaccuracies (often arising from the required simplification in the EM settings) in the output matching network.

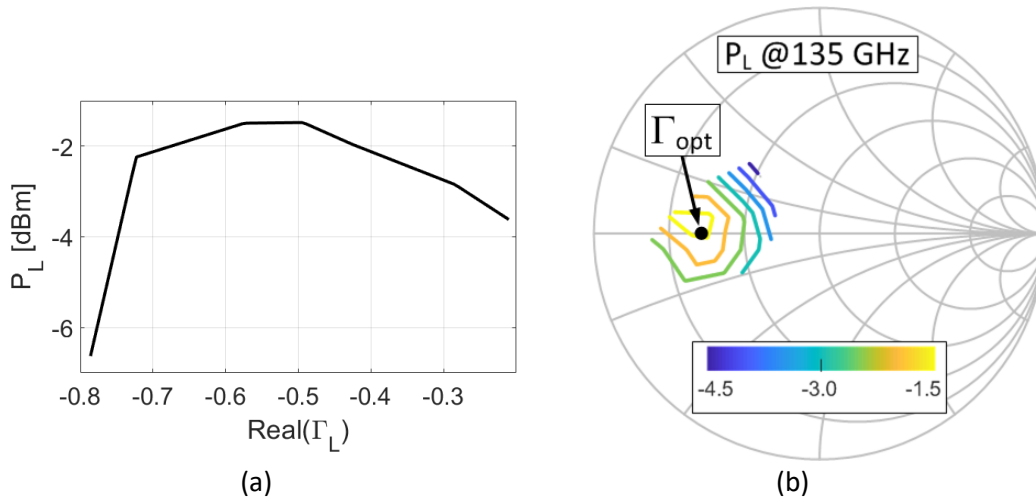


Fig. 18: Load-pull measurement results on PA reported in [16] at 135 GHz. a) Output power behavior going close to the optimum point ( $\Gamma_{opt} = -0.53$ ) to show a PL increment of around 2 dB. b) Contour plot showing the PL constant circles around the optimum point.

## 5. Conclusions

In this good practice guide, some useful analysis and practical approaches to be employed in the calibration and usage of non-50 Ohm test benches have been presented.

The analysis is focused on two (coaxial and waveguide based) test benches used in the FutureCOM project. Several insights on the peculiarities of waveguide based load-pull test benches have been detailed and metrics to enable accurate measurements have been discussed.

Some examples and related discussions have been provided on test cases of device level and PA operating in waveguide setups, i.e., above 67GHz.

## 6. Acknowledgement

The authors acknowledge support by the European Metrology Programme for Innovation and Research (EMPIR) Project 20IND03 FutureCom. This project has received funding from the EMPIR programme co-financed by the Participating States and from the European Union's Horizon 2020 research and innovation programme.

## References

- [1] Teppati V, Ferrero A, Sayed M, eds. *Modern RF and Microwave Measurement Techniques*. Cambridge University Press; 2013.
- [2] F. Mubarak, F. Munoz and M. Spirito, "A Rigorous Analysis of the Random Noise in Reflection Coefficients Synthesized via Mixed-Signal Active Tuners," 2023 101st ARFTG Microwave Measurement Conference (ARFTG), San Diego, CA, USA, 2023, pp. 1-4, doi: 10.1109/ARFTG57476.2023.10279048.
- [3] C. De Martino, L. Galatro, R. Romano, G. Parisi and M. Spirito, "Hardware and Software Solutions for Active Frequency Scalable (Sub)mm-Wave Load–Pull," in *IEEE Transactions on Microwave Theory and Techniques*, vol. 68, no. 9, pp. 3769-3775, Sept. 2020.
- [4] M. Marchetti, M. J. Pelk, K. Buisman, W. C. E. Neo, M. Spirito and L. C. N. de Vreede, "Active Harmonic Load–Pull With Realistic Wideband Communications Signals," in *IEEE Transactions on Microwave Theory and Techniques*, vol. 56, no. 12, pp. 2979-2988, Dec. 2008.
- [5] European Association of National Metrology Institutes, "Guidelines on the Evaluation of Vector Network Analyzers (VNA) - version 3.0," Tech. Rep., 2018.
- [6] F. A. Mubarak, R. Romano, L. Galatro, V. Mascolo, G. Rietveld, M. Spirito, F. A. Mubarak, and others, "Noise Behavior and Implementation of Interferometer-Based Broadband VNA," *IEEE Trans. Microw. Theory Techn.*, vol. 67, no. 1, pp. 249–260, 1 2019.
- [7] Weidman, M.P., 1995. Direct comparison transfer of microwave power sensor calibrations. NIST Technical Note 1379.
- [8] A. Ferrero and U. Pisani, "An Improved Calibration Technique for On-Wafer Large Signal Transistor Characterization", *IEEE Trans. Instrum. Meas.*, vol. IM-47, pp. 260-364, Apr. 1993.
- [9] Shan, Y. and Cui, X., 2012. RF and microwave power sensor calibration by direct comparison transfer. *Modern Metrology Concerns*, pp.175-200.
- [10] L. Galatro, S. Galbano, A. Santaniello and M. Spirito, "Power control for S-parameters and large signal characterization at (sub)-mmWave frequencies," 2015 85th Microwave Measurement Conference (ARFTG), Phoenix, AZ, USA, 2015, pp. 1-4.
- [11] Z. Aboush, J. Lees, J. Benedikt and P. Tasker, "Active harmonic load-pull system for characterizing highly mismatched high power transistors," *IEEE MTT-S International Microwave Symposium Digest*, 2005., Long Beach, CA, 2005, pp. 1311-1314.
- [12] A. Ferrero, V. Teppati and A. Carullo, "Accuracy evaluation of on-wafer load-pull measurements," in *IEEE Transactions on Microwave Theory and Techniques*, vol. 49, no. 1, pp. 39-43, Jan. 2001.
- [13] V. Teppati, A. Ferrero, D. Parena and U. Pisani, "Accuracy Improvement of Real-Time Load-Pull Measurements," in *IEEE Transactions on Instrumentation and Measurement*, vol. 56, no. 2, pp. 610-613, April 2007.
- [14] T. J. Reck et al., "Micromachined Probes for Submillimeter-Wave On-Wafer Measurements—Part II: RF Design and Characterization," in *IEEE Transactions on Terahertz Science and Technology*, vol. 1, no. 2, pp. 357-363, Nov. 2011.
- [15] M. Spirito, M. J. Pelk, F. van Rijs, S. J. C. H. Theeuwes, D. Hartskeerl and L. C. N. de Vreede, "Active Harmonic Load–Pull for On-Wafer Out-of-Band Device Linearity Optimization," in *IEEE Transactions on Microwave Theory and Techniques*, vol. 54, no. 12, pp. 4225-4236, Dec. 2006.
- [16] Z. Hu, G. Sarris, C. De Martino, M. Spirito and E. McCune, "Design and linearity analysis of a D-band power amplifier in 0.13  $\mu\text{m}$  SiGe BiCMOS technology," 2017 IEEE Compound Semiconductor Integrated Circuit Symposium (CSICS), Miami, FL, 2017, pp. 1-4.